The Astrophysical Journal Letters, 903:L23 (8pp), 2020 November 1 https://doi.org/10.3847/2041-8213/abc0e8

Particle-in-cell Simulation of Whistler Heat-flux Instabilities in the Solar Wind: Heat-flux Regulation and Electron Halo Formation

A. Micera[1,2], A. N. Zhukov[1,3], R. A. López[4], M. E. Innocenti[5], M. Lazar[2,5], E. Boella[6,7], and G. Lapenta[2]
[1] Solar-Terrestrial Centre of Excellence—SIDC, Royal Observatory of Belgium, Brussels, Belgium
[2] Centre for Mathematical Plasma Astrophysics, KU Leuven, Leuven, Belgium
[3] Skobeltsyn Institute of Nuclear Physics, Moscow State University, Moscow, Russia
[4] Departamento de Física, Universidad de Santiago de Chile, Santiago, Chile
[5] Institut für Theoretische Physik, Ruhr-Universität Bochum, Bochum, Germany
[6] Physics Department, Lancaster University, Lancaster, UK
[7] Cockcroft Institute, Daresbury Laboratory, Warrington, UK
Received 2020 July 29; revised 2020 October 6; accepted 2020 October 14; published 2020 November 2

Abstract

We present results of a two-dimensional fully kinetic particle-in-cell simulation in order to shed light on the role of whistler waves in the scattering of strahl electrons and in the heat-flux regulation in the solar wind. We model the electron velocity distribution function as initially composed of core and strahl populations as typically encountered in the near-Sun solar wind as observed by Parker Solar Probe. We demonstrate that, as a consequence of the evolution of the electron velocity distribution function (VDF), two branches of the whistler heat-flux instability can be excited, which can drive whistler waves propagating in the direction oblique or parallel to the background magnetic field. First, oblique whistler waves induce pitch-angle scattering of strahl electrons, toward higher perpendicular velocities. This leads to the broadening of the strahl pitch-angle distribution and hence to the formation of a halo-like population at the expense of the strahl. Later on, the electron VDF experiences the effect of parallel whistler waves, which contributes to the redistribution of the particles scattered in the perpendicular direction into a more symmetric halo, in agreement with observations. Simulation results show a remarkable agreement with the linear theory of the oblique whistler heat-flux instability. The process is accompanied by a significant decrease of the heat flux carried by the strahl population.

Unified Astronomy Thesaurus concepts: Solar wind (1534); Space plasmas (1544); Plasma astrophysics (1261)

1. Introduction

Electron velocity distribution functions (VDFs) in the solar wind often consist of three components. At lower energies, there is a dense, thermal, and almost isotropic core, while at higher energies, a suprathermal halo population is distributed at all pitch angles and a suprathermal field-aligned strahl can be observed (Feldman et al. 1975; Pilipp et al. 1987; Gosling et al. 2001; Salem et al. 2003; Stverák et al. 2009; Halekas et al. 2020).

This peculiar nonthermal structure of the electron VDF carries an important amount of heat flux in the solar wind (Marsch 2006). In situ observations made at 1 au (Feldman et al. 1976; Bale et al. 2013) and farther away from the Sun (Scime et al. 1994) show that the heat flux carried by the solar wind is suppressed below the values provided by collisional models (Spitzer & Härm 1953). Since suprathermal electron populations are not affected much by Coulomb collisions (the Coulomb cross section strongly depends on the particle velocities), a wide variety of kinetic instabilities can be responsible for shaping the electron VDF, reducing the skewness of suprathermal features in the distribution, and hence regulating the heat flux (e.g., Gary et al. 1975, 1994; Scime et al. 1994; Lazar et al. 2011; Roberg-Clark et al. 2019).

Recent observations by the Parker Solar Probe (PSP) mission have shown that in the vicinity of the Sun the halo fractional density represents only a very small percentage of the total electron density, while the strahl is more pronounced (Berčič et al. 2020; Halekas et al. 2020). Furthermore, while the halo fractional density increases with the heliocentric distance, the strahl fractional density decreases (Hammond et al. 1996; Maksimovic et al. 2005; Pagel et al. 2007; Stverák et al. 2009; Anderson et al. 2012; Gurgiolo et al. 2012; Berčič et al. 2019). These observations suggest that the formation of the halo population takes place from pitch-angle scattering of the strahl as the solar wind expands (Pierrard & Lemaire 1996; Maksimovic et al. 1997; Landi & Pantellini 2003; Boldyrev & Horaites 2019; Tang et al. 2020).

Since deviations from the thermal distribution are more pronounced in the weakly collisional fast solar wind (Ogilvie & Scudder 1978; Phillips & Gosling 1990; Landi & Pantellini 2003), and considering that the major part of the heat flux in the fast solar wind is carried by the strahl electrons (Rosenbauer et al. 1977; Pilipp et al. 1987), the heat-flux suppression and the density exchange between the high-energy components of the electron VDF are two related mechanisms that are fundamental to understand the dynamic of the solar wind at the early stages of its expansion. One of the models often invoked in this respect assumes a fundamental role of whistler-mode waves, generated by electron-driven instabilities. Indeed, in the presence of counter-streaming electron populations, parallel and oblique (with respect to the interplanetary magnetic field) whistler-like fluctuations can be excited by self-generated microinstabilities (Gary et al. 1975). Observations confirm the existence of quasi-parallel whistler fluctuations in the solar wind at 1 au (Lacombe et al. 2014) and in the pristine solar wind (Tong et al. 2019). Moreover, recent PSP data, collected in the inner heliosphere, revealed the existence of whistler-mode waves with a polarization range that goes from parallel to highly oblique (Agapitov et al. 2020; Cattell et al. 2020; Malaspina et al. 2020; Mozer et al. 2020).

It has long been debated whether collisional or collisionless processes are mainly responsible for the heat-flux reduction in the solar wind (e.g., Marsch 2006). Halekas et al. (2020) analyzed the first data of the PSP mission and found a better correlation of the strahl and halo fractional densities with the electron-core plasma β, with β being the ratio of the thermal pressure to the magnetic pressure, rather than with the collisional age. This suggests that in the near-Sun solar wind the regulation of the nonthermal features of the electron VDF and hence of the electron heat flux may be carried out predominantly by wave–particle interactions rather than by collisions.

One-dimensional particle-in-cell (PIC) simulations aimed at reproducing the interactions between electron VDFs and parallel whistler waves, generated by whistler heat-flux instability (WHFI) in solar wind conditions, have recently been performed (e.g., Kuzichev et al. 2019; López et al. 2019). Furthermore, theoretical studies on the effects of highly oblique whistler waves in suppressing the electron heat flux and in transferring the strahl electrons into the halo have been carried out (Vasko et al. 2019; Verscharen et al. 2019).

López et al. (2020) explored the various possible heat-flux-related instabilities and their relevance depending on the solar wind conditions. Innocenti et al. (2020) have shown via fully kinetic expanding box model simulations (Innocenti et al. 2019a, 2019b) that the solar wind expansion can trigger or modify the evolution of kinetic microinstabilities that can in turn affect the heat-flux regulation. However, it remains an open question whether whistler heat-flux instabilities and the resulting wave fluctuations can correctly describe the reasons why the strahl fractional density decreases with heliocentric distance and whether they can explain the low level of electron heat flux inconsistent with the Spitzer–Härm predictions (Spitzer & Härm 1953).

Here, we present kinetic simulations of the full spectrum of whistler-like fluctuations, self-generated by two drifting electron populations, without seeding any instability and without imposing a temperature gradient. We initialize core–strahl electron VDFs, characteristic of the near-Sun solar wind, and we address, via a nonlinear analysis, the process responsible for reducing the strahl drift velocity, for the generation of the electron halo population from pitch-angle scattering of strahl electrons, and for regulating the electron heat flux.

This Letter is organized as follows. Section 2 illustrates the simulation setup. Section 3 reports the first two-dimensional (2D) simulation of the whistler heat-flux instabilities triggered by a realistic solar wind electron VDF. Section 4 presents a discussion of the simulation results and reports the conclusions.

2. Setup of the PIC Simulation

In order to provide a complete picture of the nonlinear interaction between suprathermal electrons and whistler waves, and to determine the effects of those waves on the heat flux carried by the solar wind, we perform a 2D full PIC simulation using the semi-implicit code, iPIC3D (Markidis et al. 2010).

We model a collisionless plasma with initially uniform background magnetic field. The plasma and magnetic field parameters correspond to those measured by PSP during its first perihelion by the SWEAP (Kasper et al. 2019) and FIELDS (Bale et al. 2019) instruments, as reported by Halekas et al. (2020). The magnetic field is directed along the x-axis, $\boldsymbol{B}_0 = B_0\hat{e}_x$. Its magnitude $B_0 = 60$ nT is such that $v_{Ae}/c = 0.01$, with $v_{Ae} = B_0/\sqrt{4\pi n_e m_e}$ being the electron Alfvén speed, n_e is the electron number density, m_e is the electron mass, and c is the speed of the light in vacuum. The plasma is composed of core (subscript c) and strahl (subscript s) electrons, and ions (subscript i), assumed to be only protons, with real mass ratio $\mu = m_i/m_e = 1836$. We use 2048 particles per cell per species. The plasma satisfies the quasi-neutrality condition: $n_i = n_e = n_c + n_s$, where n_i, $n_c = 0.95\,n_e$ and $n_s = 0.05\,n_e$ are the ion, electron-core, and electron-strahl densities, respectively. The electron core is characterized by a sunward drift that balances the current carried by the strahl (Feldman et al. 1975; Scime et al. 1994): $n_c u_c + n_s u_s = 0$, with $u_c(u_s)$ electron-core (electron-strahl) drift velocity. We select an initial strahl drift velocity $u_s = 3.1\,v_{Ae}$, and hence $u_c = -0.16\,v_{Ae}$ in order to satisfy the zero net-current condition.

The initial number density is $n_e = 350$ cm^{-3}. The temperature of the core is $k_B T_c = 43$ eV, where k_B is the Boltzmann constant, such that $\beta_c = 1.6$, with $\beta_j = 8\pi n_j k_B T_j/B_0^2$. Regarding the ions, we assume that their drift velocity is zero ($u_i = 0$) and $\beta_i = 2$. Core electrons and ions are assumed initially isotropic ($T_{j,\perp}/T_{j,\parallel} = 1$) and Maxwellian.

For the strahl we adopt a temperature in the direction parallel to the background magnetic field of $k_B T_{s,\parallel} = 179$ eV, a temperature anisotropy $T_{s,\parallel}/T_{s,\perp} = 2$ (to take into account the limited angular extent of the strahl in PSP observations (Berčič et al. 2020), and the adiabatic focusing of the strahl in the expanding solar wind). The initial VDF is thus a drifting bi-Maxwellian:

$$f_j(v_\parallel, v_\perp, t=0) = \frac{(2\pi)^{-3/2}}{w_{\perp j}^2 w_{\parallel j}} \exp\left(-\frac{v_\perp^2}{2w_{\perp j}^2} - \frac{(v_\parallel - u_j)^2}{2w_{\parallel j}^2}\right), \quad (1)$$

with $w_j = \sqrt{k_B T_j/m_j}$ being the thermal velocity of the species j, while $\perp$ and $\parallel$ denote directions perpendicular and parallel to the background magnetic field, $\boldsymbol{B}_0$, with $v_\parallel \equiv v_x$. The use of a drifting-Maxwellian or a drifting-bi-Maxwellian model to describe the core and the strahl, respectively, is motivated by the PSP observations of near-Maxwellian VDFs, for both electron populations, close to the Sun (Berčič et al. 2020; Halekas et al. 2020). The resulting initial VDF is shown in Figure 1(a).

With these parameters, we obtain $\omega_{pe}/\Omega_{ce} = 100$, with $\omega_{pe} = \sqrt{4\pi e^2 n_e/m_e}$ and $\Omega_{ce} = eB_0/m_e c$ being the plasma and the cyclotron frequencies for the electrons, respectively, and e is the elementary charge.

A square simulation box with length $L = 8\,d_i$ has been employed, where $d_i = c/\omega_{pi}$ is the ion inertial length, with $\omega_{pi} = \sqrt{4\pi e^2 n_i/m_i}$ being the plasma frequency for the ions. A cell size $\Delta x = \Delta y = 0.01\,d_i$ and a temporal step $\Delta t = 0.05\,\omega_{pi}^{-1}$ have been chosen. The ion cyclotron frequency is $\Omega_{ci} = eB_0/m_i c = 0.000233\,\omega_{pi}$.

We note that simulations performed with different resolutions and numbers of particles per cell yield similar results, confirming code convergence.

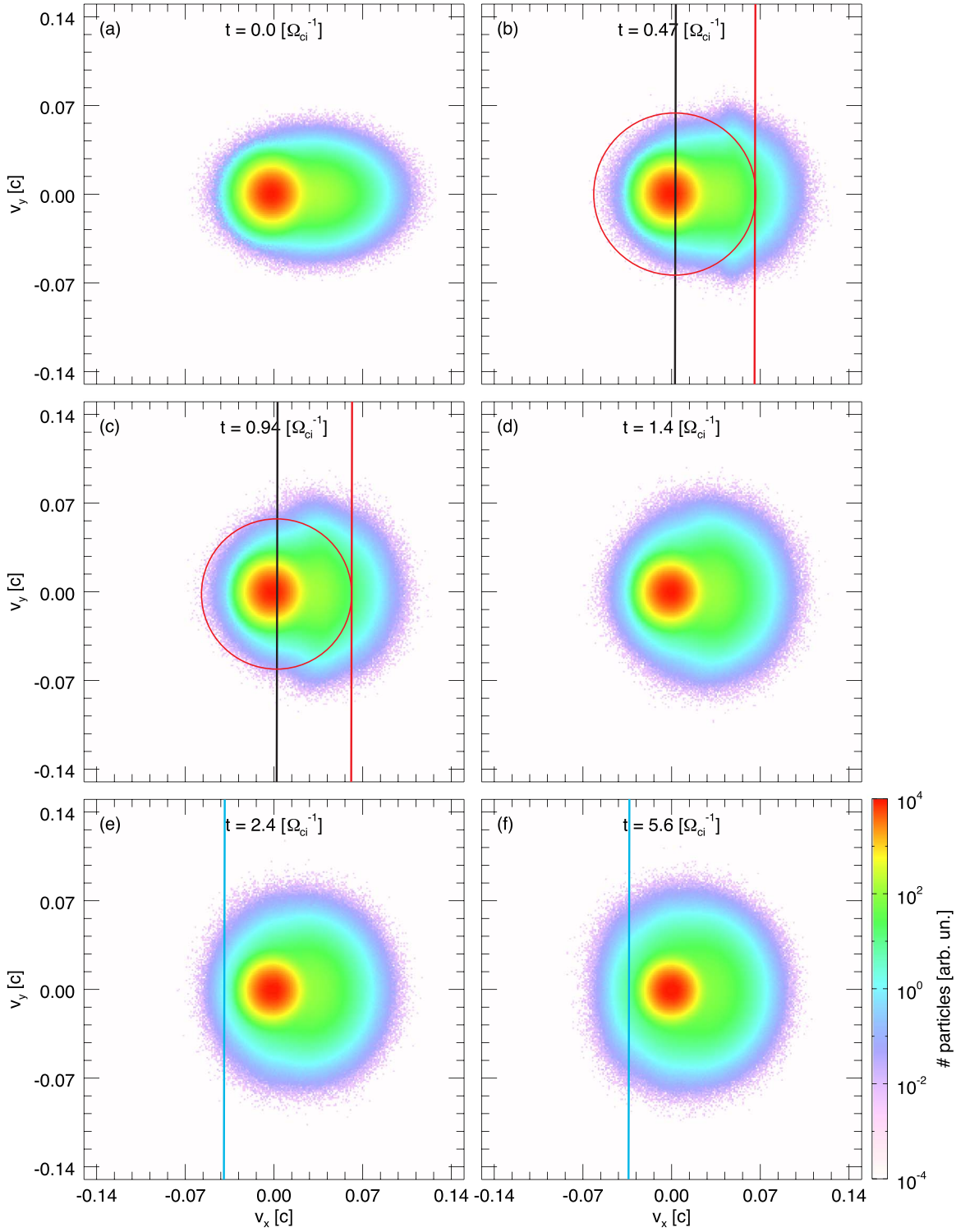

Figure 1. Electron VDF $f_e = f(v_x, v_y)$ at $t_0 = 0$ (initial distribution, panel (a)), $t_1 = 0.47$ (linear stage of O-WHFI, panel (b)), $t_2 = 0.94$ (O-WHFI relaxation, panel (c)), $t = 1.4$ (O-WHFI saturation, panel (d)), $t = 2.4$ (quasi-parallel WHFI, panel (e)), and $t_{\rm end} = 5.6$ (final stage, panel (f)). The time is in units of Ω_{ci}^{-1}. Black and red vertical lines in panels (b) and (c) indicate $v_\parallel$ values at which $n = 0$ and $n = 1$ resonances of oblique whistler waves are expected, while circles show electron diffusion paths due to the $n = 1$ resonance interaction. Cyan vertical lines in panels (e) and (f) indicate $v_\parallel$ values at which $n = -1$ resonance is expected.

3. Simulation Results

Various types of heat-flux-related instabilities can be triggered in the presence of two counter-streaming populations of electrons, according to the initial parameters. Namely, these are the quasi-parallel WHFI (Gary et al. 1975), the firehose heat-flux instability (Shaaban et al. 2018), the oblique whistler heat-flux instability (O-WHFI) (López et al. 2020), or electrostatic instabilities of the electron acoustic or electron beam modes (Gary 1978). For the plasma parameters employed in our simulation, the system is initially subject to the oblique whistler heat-flux instability. This is a right-hand polarized mode with maximum growth rate at the oblique angle of

propagation. This instability has gained renewed attention due to recent PSP observations of oblique whistler waves in the solar wind near the Sun (e.g., Agapitov et al. 2020; Cattell et al. 2020).

Figure 1 depicts the the total electron VDF $f_e = f(v_x, v_y)$ at the initial stage of the simulation ($t_0 = 0$; Figure 1(a)), during the development of the oblique whistler heat-flux instability (Figures 1(b) and (c), respectively, at $t_1 = 0.47\ \Omega_{ci}^{-1}$ and $t_2 = 0.94\ \Omega_{ci}^{-1}$), after the O-WHFI saturation (Figure 1(d)), during the development of the quasi-parallel WHFI (Figure 1(e)) and at the final stage ($t_{\rm end} = 5.6\ \Omega_{ci}^{-1}$) of the simulation (Figure 1(f)). The strahl undergoes pitch-angle scattering (by the excited whistler waves, as will be shown below), which results in the reduction of the strahl drift velocity and in the simultaneous broadening of the strahl pitch-angle distribution (Figure 1(b)). The scatter of the strahl electrons leads to the formation of a new population that can be seen as a halo, whose features are noticeable in the electron VDF from the onset of the O-WHFI to the final stages of the simulation (Figure 1(e)).

To give further evidence of the halo formation, in Figures 2(a) and (b) we compare the cuts of the total electron VDF along the parallel (f_e (v_x, $v_y = 0$)) and perpendicular (f_e ($v_x = 0$, v_y)) directions, for the times shown in Figure 1. One can observe the presence of the strahl component along the magnetic field direction, the relaxation of its drift velocity, and the appearance of the suprathermal halo, which, at higher energies, deviates from the Maxwellian distribution. In Figures 2(c) and (d) we show the temporal variation of the total electron VDF as can be seen from the ratios $f_e(t_2)/f_e(t_0)$ and $f_e\ (t_{\rm end})/f_e\ (t_2)$, respectively, while in Figures 2(e) and (f) we show the temporal variations of the strahl VDF: $f_s\ (t_2) - f_s\ (t_0)$ and $f_s\ (t_{\rm end}) - f_s\ (t_2)$, respectively. All four panels confirm the generation of suprathermal halo particles distributed at all pitch angles at the expense of the strahl.

In Figures 3(a) and (b) we report the growth rates γ and the corresponding real wave frequencies ω_r in the $k_x k_y$ plane, obtained from the theoretical linear dispersion relation. The strongest instability induced by the core–strahl electron VDF is the purely oblique right-handed O-WHFI, with maximum growth rate $\gamma_{\rm max} \approx 12.5\ \Omega_{ci}$ at $k_x \approx 6.5\ \omega_{pi}/c$ and $k_y \approx 13.5\ \omega_{pi}/c$. The unstable whistler modes have frequencies in the range of $\Omega_{ci} < \omega_r < \Omega_{ce}$ and present their maximum growth rate at $\theta \approx 65°$.

The simulation clearly exhibits evidence of this instability. Indeed, the fast Fourier transform (FFT) of the simulated transverse magnetic fluctuations, normalized to the background magnetic field (FFT($\delta B_z/B_0$)), at $t_1 = 0.47\ \Omega_{ci}^{-1}$ displayed in Figure 3(c), shows that the power is concentrated at highly oblique angles, $k_y \approx 13\ \omega_{pi}/c$, and between $k_x = 6$ and $8\ \omega_{pi}/c$. At $t_{\rm end} = 5.6\ \Omega_{ci}^{-1}$, when the O-WHFI is already saturated, we observe weak modes that are mainly parallel or quasi-parallel to the background magnetic field; see Figure 3(d). These fluctuations concentrate at higher parallel wavenumbers, between $k_x = 11$ and $13\ \omega_{pi}/c$, characteristic of the quasi-parallel WHFI. The transition from oblique to parallel modes is confirmed in Figures 3(e) and (f), where we show the transverse magnetic field in the xy plane at $t_1 = 0.47\ \Omega_{ci}^{-1}$ and $t_{\rm end} = 5.6\ \Omega_{ci}^{-1}$, respectively.

The evolution of the fastest-growing mode, at $k_x = 6.5\ \omega_{pi}/c$ and $k_y = 13.5\ \omega_{pi}/c$, obtained from the simulation, shows an exponential growth that saturates at $t \approx 0.6\ \Omega_{ci}^{-1}$, followed by a relaxation, as shown in Figure 4(a). The maximum growth rate according to the linear theory is very similar to that obtained in our simulation. In Figure 4(a) we also show the temporal evolution of a parallel whistler mode selected through a cut of FFT($\delta B_z/B_0$) at $k_x = 12\ \omega_{pi}/c$ and $k_y = 0$. Parallel and quasi-parallel modes are manifested at later times and become dominant after $t \approx 2\ \Omega_{ci}^{-1}$.

The scattering of the strahl electrons by the generated whistler waves provokes the saturation of the O-WHFI instability, but, at this point, the newly generated halo provides the energy for the excitation of quasi-parallel whistler waves (see Figure 3(d)). A further portion of suprathermal electrons is scattered by the enhanced quasi-parallel whistler fluctuations and the process results in a consequent relaxation of the strahl drift velocity, in the formation of a more symmetric halo, and leads to a more isotropic total electron VDF.

To explore the physical nature of the strahl electron scattering, we investigate the resonance conditions. In Figures 1(b) and (c), the black and red vertical lines identify the parallel velocities at which the $n = 0$ (Landau) and $n = 1$ (cyclotron) resonant interactions of the fastest-growing whistler wave with electrons are expected, calculated as $v_\parallel = (n\,\Omega_{ce} + \omega_r)/k_\parallel$, while circles show the electrons diffusion paths due to the $n = 1$ resonance interaction, as constant energy surfaces in the wave frame of reference (Verscharen et al. 2019). The circles are centered at $v_\parallel = v_{\rm ph}$ and $v_\perp = 0$, with $v_{\rm ph} = \omega_r/k_\parallel$ being the parallel phase velocity of the waves. The $k_\parallel$, which in our simulation corresponds to k_x of the fastest-growing wave, is computed via FFT in the space of the transverse magnetic fluctuations (see Figures 3(c) and (d)), while ω_r is obtained from the linear dispersion relation (see Figure 3(b)) for $k_\parallel$ and $k_\perp$ of the fastest-growing wave. We consider the variation of $k_\parallel$ during the development of the O-WHFI, and we take $k_\parallel = 6.5\ \omega_{pi}/c$ at $t_1 = 0.47\ \Omega_{ci}^{-1}$ and $k_\parallel = 8\ \omega_{pi}/c$ at $t_2 = 0.94\ \Omega_{ci}^{-1}$. The red vertical lines, respectively drawn at $v_\parallel = 0.068\ c$ in Figure 1(b) and $v_\parallel = 0.057\ c$ in Figure 1(c), delineate the electron population that fulfills the $n = 1$ resonance condition and diffuses, via pitch-angle scattering, toward higher values of $v_\perp$. Indeed, in both panels, the circles closely correspond to the non-Maxwellian horn-like structures of the electron VDF (around $v_x = 0.05\ c$ at $t = t_1$ and around $v_x = 0.035\ c$ at $t = t_2$). The Landau resonance ($n = 0$) is not prominent in the $v_\parallel > 0$ region of the VDF in the early stage of the simulation as $\partial f_e/\partial v_\parallel < 0$. However, on the left side of horn-like extensions we see $\partial f_e/\partial v_\parallel > 0$, so the Landau resonance starts to be effective when the horns reach the black vertical line (around $t_2 = 0.94\ \Omega_{ci}^{-1}$). The Landau resonance scatters electrons along $v_\parallel$, contributing to the isotropization of the scattered electrons and the formation of the electron halo. The generation of the tail in the distribution function at $v_\parallel < 0$ (see also Figures 2(a) and (d)) can be traced back to the $n = -1$ cyclotron resonance (Roberg-Clark et al. 2019; Verscharen et al. 2019) that the electron VDF experiences later in time, when there is a sufficient number of electrons with $v_x < 0$ and quasi-parallel WHFI is triggered. Particles with high $v_\perp$ that fulfill this resonant condition are scattered by waves toward lower values of v_x (in the direction opposite to B_0), leading to the formation of a more symmetric halo. In Figures 1(e) and (f) the cyan vertical lines indicate $v_\parallel$ values at which $n = -1$ resonance interactions of electrons with quasi-parallel whistler waves are expected. The ω_r values, at these stages, are obtained by solving the linear dispersion

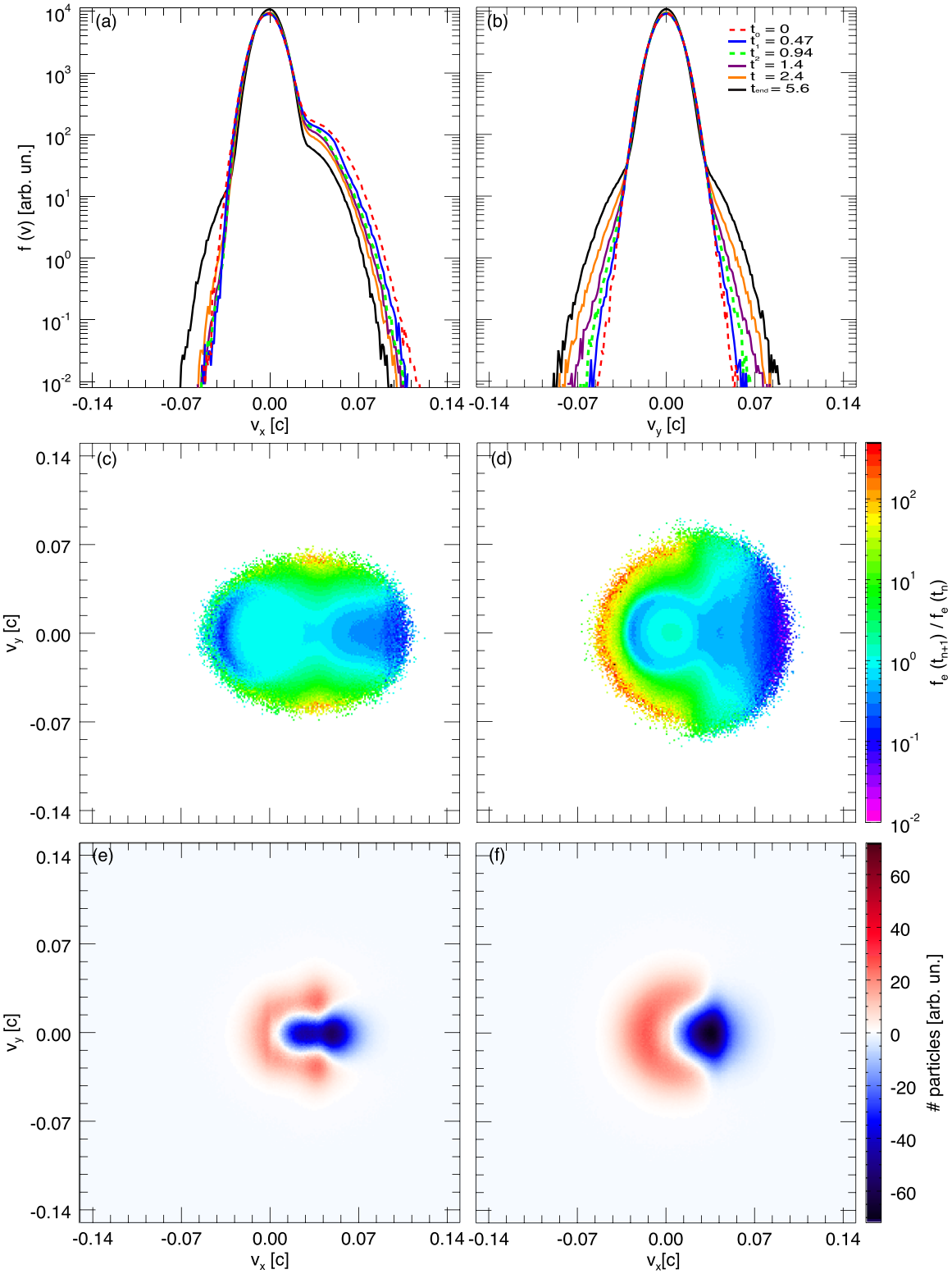

Figure 2. Total electron VDF cuts along the parallel (f_e (v_x, $v_y = 0$, panel (a)) and perpendicular (f_e ($v_x = 0$, v_y, panel (b)) directions. Colored lines indicate the cuts of the VDFs at different times. Temporal variations of the total electron VDF: f_e (t_2)/f_e (t_0) (panel (c)) and f_e ($t_{\rm end}$)/f_e (t_2) (panel (d)). Variations of the strahl distribution function: f_s (t_2) − f_s (t_0) (panel (e)) and f_s ($t_{\rm end}$) − f_s (t_2) (panel (f)).

relation for the parallel whistler instability triggered by the isotropic drifting suprathermal population of electrons.

In Figures 4(b)–(d) we display the temporal evolution of the strahl drift velocity u_s and the heat flux Q_s carried by the strahl along the magnetic field direction. Since the drift velocities of the core and the strahl are initialized in the parallel direction with respect to the magnetic field, the parallel component of the heat flux carried by the strahl in the reference frame of the solar wind (strahl energy flux) is dominant compared to the perpendicular components. It is determined by $Q_s = \frac{m_s}{2}\int v_\parallel v^2 f_s d^3v$ and it can

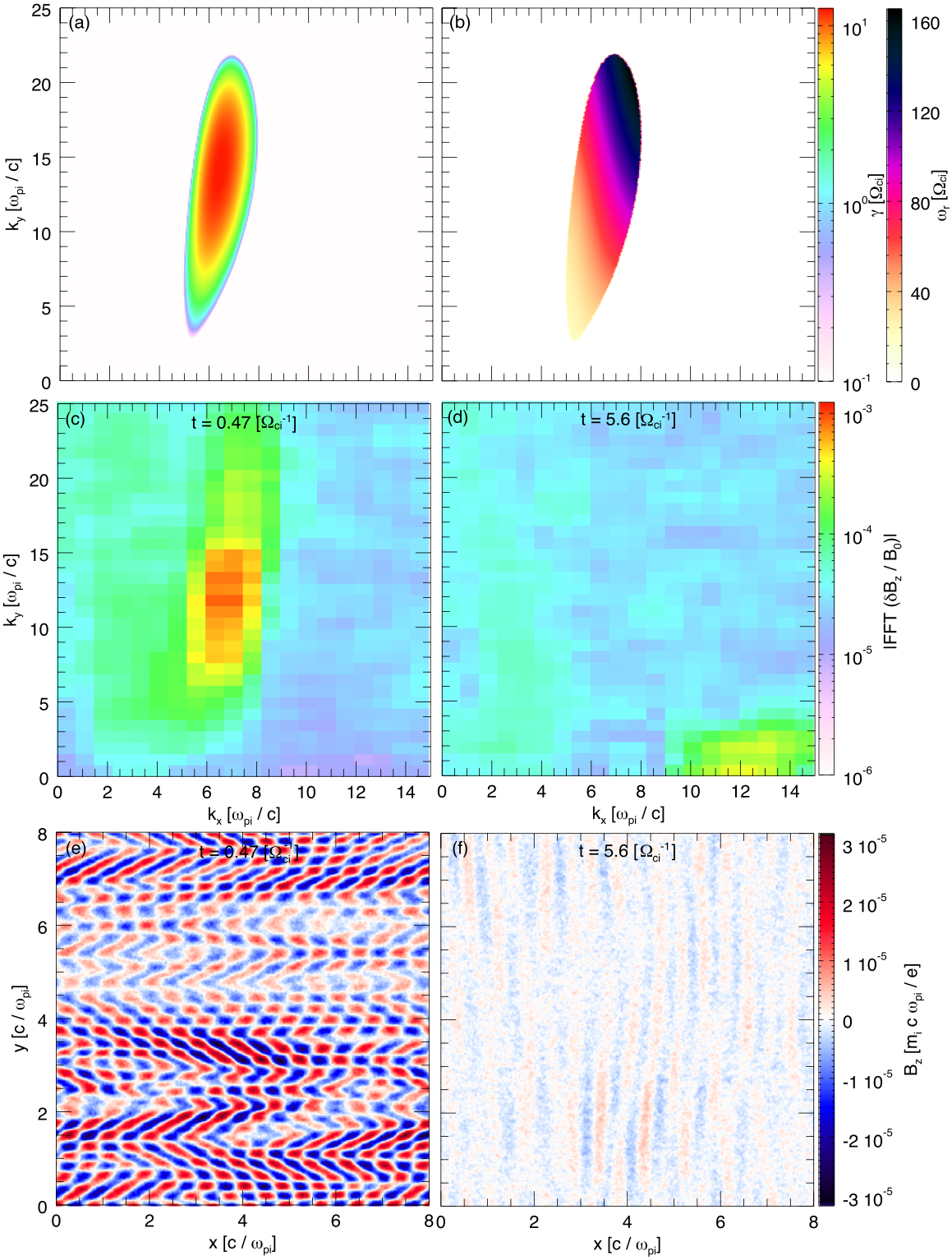

Figure 3. Oblique whistler heat-flux instability growth rates γ (a) and wave frequencies $_r$ (b) in the k_x–k_y plane obtained from the linear dispersion relation. Fast Fourier transforms of the simulated transverse magnetic fluctuations FFT($\delta B_z/B_0$) at $t_1 = 0.47\ \Omega_{ci}^{-1}$ (c) and $t_{\rm end} = 5.6\ \Omega_{ci}^{-1}$ (d). B_z component (color scale) in the x–y plane at $t_1 = 0.47\ \Omega_{ci}^{-1}$ (e) and $t_{\rm end} = 5.6\ \Omega_{ci}^{-1}$ (f).

be broken into several components (Feldman et al. 1975; Innocenti et al. 2020) as $Q_s = Q_{{\rm enth},s} + Q_{{\rm bulk},s} + q_s$, where $Q_{{\rm enth},s} = \frac{3}{2} n_s m_s u_s w_s^2$ reflects the convection of the strahl electron enthalpy, $Q_{{\rm bulk},s} = \frac{1}{2} m_s n_s u_s^3$ is the energy flux due to the bulk motion of the electrons, and $q_s = \frac{m_s}{2}\int (v_\parallel - u_s)(v - u_s)^2 f_s\, d^3v$ represents the heat flux carried by the strahl in its reference frame (skewness of the strahl VDF). The decrease of the strahl energy flux is around 46% during the entire simulation. Comparison of Figures 4(a), (b), and (c) shows that the strongest heat-flux rate decrease is simultaneous with the growth of the oblique wave modes and the consequent decrease of the strahl drift velocity that

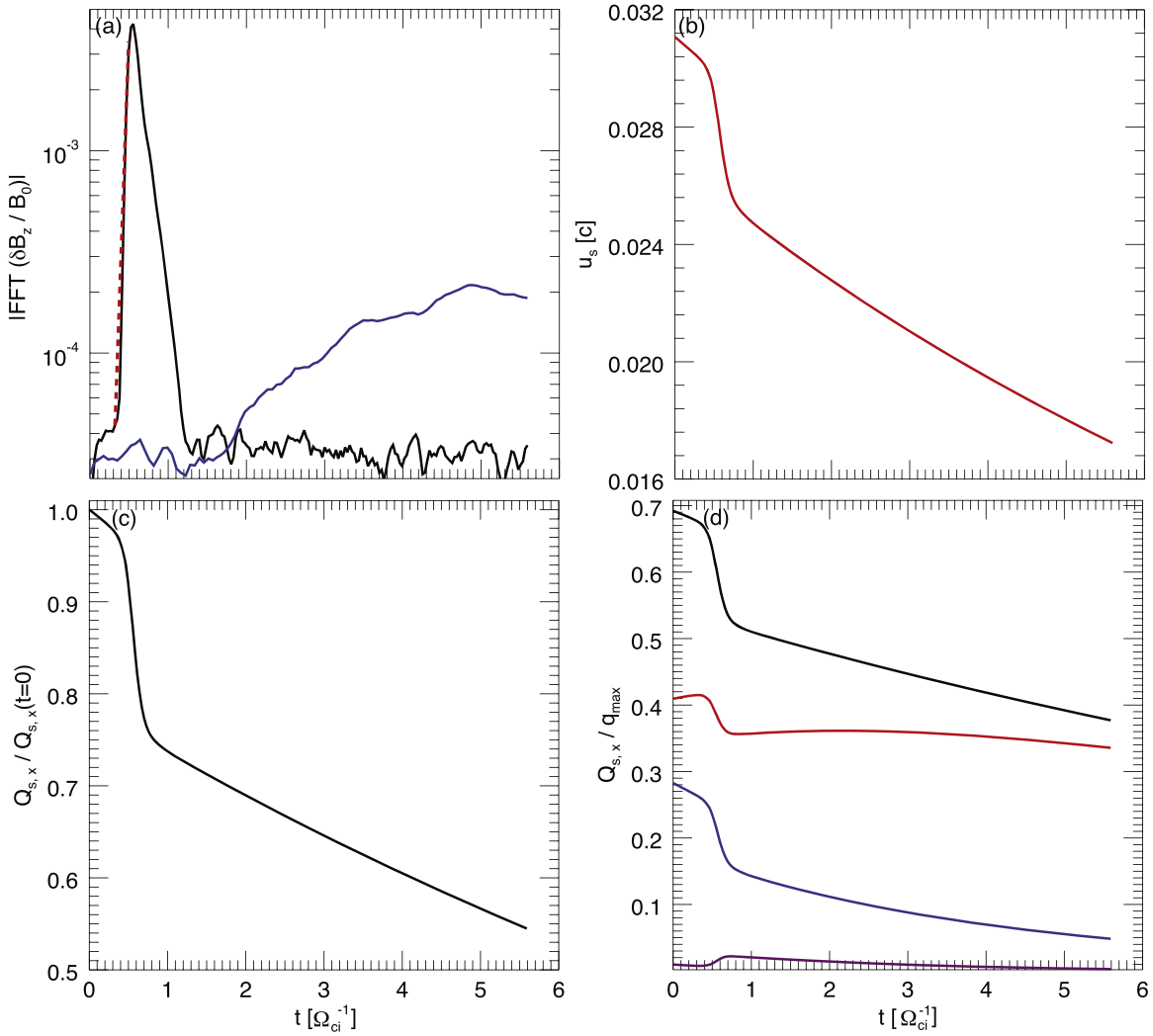

Figure 4. Temporal evolution of the simulated fastest-growing oblique mode ($k_x = 6.5\ \omega_{pi}/c$ and $k_y = 13.5\ \omega_{pi}/c$, solid black line), of the simulated parallel mode at $k_x = 12\ \omega_{pi}/c$ and $k_y = 0$ (solid blue line), and comparison with the maximum theoretical growth rate ($\gamma_{\max} = 12.5\ \Omega_{ci}$, red dashed line) (a). Temporal evolution of parallel strahl drift velocity u_s (b) and of strahl energy flux normalized to its initial value Q_s/Q_s ($t = 0$) (c). Energy flux components carried by the electron strahl along the magnetic field direction: Q_s (black), $Q_{\mathrm{enth},s}$ (red), $Q_{\mathrm{bulk},s}$ (blue), and q_s (purple) (d). All the energy flux components are normalized to $q_{\max} = 5/2 m_e (n_c w_c^3 + n_s w_s^3)$.

it produces, and it lasts until their saturation. After the O-WHFI is already saturated, the plasma is still unstable to the quasi-parallel WHFI (as shown in Figure 3) and then the heat flux is subject to a further decrease. It is important to note that the rate of reduction of the heat flux, due to the O-WHFI (before $t \approx 0.8\ \Omega_{ci}^{-1}$), is almost one order of magnitude higher than the rate of the heat flux reduction due to quasi-parallel wave modes. The heat flux is mostly carried by the convection of the strahl electron enthalpy, indicated in Figure 4(d) with a red line, in agreement with the observations reported by Feldman et al. (1975). The regulation of the global strahl energy flux Q_s along the background magnetic field is essentially produced by the relaxation of the strahl drift velocity rather than by the variation of the thermal velocity w_j similarly to the results reported in Innocenti et al. (2020). The heat flux carried by the strahl in its reference frame represents a small part of the total energy flux. However it exhibits an increase when oblique whistler waves interact with the electron VDF and then a reduction due to the scatter of the strahl trough lower drift velocities, as q_s is a direct measure of the electron VDF deformation.

4. Discussion and Conclusions

We perform a 2D fully kinetic simulation to investigate the role of the oblique and parallel branches of whistler heat-flux instability in shaping the electron VDFs in the solar wind. We confirm that, in a plasma consisting of a drifting core and strahl electrons, as recently observed by PSP in the near-Sun solar wind, whistler waves, propagating at oblique angles with respect to the background magnetic field, can be excited, in agreement with Verscharen et al. (2019) and López et al. (2020). The free energy of the counter-streaming populations of electrons is converted into magnetic energy in the form of oblique whistler-mode waves that produce an enhanced and rapid suppression of the plasma heat flux until their saturation. The oblique whistler waves also drive a significant pitch-angle scattering of the field-aligned strahl, which results in the formation of a suprathermal electron halo population. A portion of the strahl population of electrons, whose parallel velocities satisfy the $n = 1$ cyclotron resonance condition, is scattered toward high values of perpendicular velocities, producing strong deviations of the VDF from the original distribution.

Our nonlinear study allows us to conclude that the excited whistler-mode waves shift toward smaller angles of propagation as the bulk velocity of the strahl decreases and that the diffusion of the electrons to higher $v_\perp$ occurs mostly during the linear and nonlinear stages of the oblique whistler heat-flux instability. During the nonlinear stage, the scattering of electrons in the parallel direction starts, at least partly due to the $n = 0$ Landau resonance with the oblique whistler waves. Later on, when there is a sufficient number of suprathermal electrons with $v_x < 0$, the electron system experiences secondary effects due to the $n = -1$ cyclotron resonant interaction with parallel whistler waves. Even if the parallel modes saturate at moderate levels of magnetic field fluctuations and reduce the heat flux only slowly, they do lead to a further relaxation of the suprathermal electrons, to the generation of a tail-like structure in the distribution function at $v_x < 0$ and hence to a more symmetric halo, in agreement with observations.

We notice that while modeling the initial distribution function of the strahl population as a drifting bi-Maxwellian provides an accurate representation for pristine solar wind conditions (Berčič et al. 2020; Halekas et al. 2020), it may not be accurate at large heliocentric distances. In this case, simulations should be initialized with a different distribution function (e.g., Horaites et al. 2018). The study of the WHFI for non-Maxwellian strahl VDF is more relevant close to the Earth and is beyond the scope of this work.

Future in situ observations by PSP at even smaller heliocentric distances may further clarify the physical processes affecting the electrons, since in the close vicinity of the Sun, before the propagation through the heliosphere, electron VDFs are less affected by different microinstabilities. This may give us an opportunity to detect pristine electron VDFs and thus gain an insight into the processes that influence solar wind particle distributions at the early stages of their evolution.

The authors thank J. S. Halekas for helpful discussions. This work was supported by a PhD grant awarded by the Royal Observatory of Belgium to one of the authors (A.M.). These simulations were performed on the supercomputers SuperMUC (LRZ) and Marconi (CINECA) under PRACE allocations. A. N.Z. thanks the European Space Agency (ESA) and the Belgian Federal Science Policy Office (BELSPO) for their support in the framework of the PRODEX Programme. R.A.L thanks the support of AFOSR grant FA9550-19-1-0384. M.E. I.'s work is supported by an FWO postdoctoral fellow.

ORCID iDs

A. Micera https://orcid.org/0000-0001-9293-174X
A. N. Zhukov https://orcid.org/0000-0002-2542-9810
R. A. López https://orcid.org/0000-0003-3223-1498
M. E. Innocenti https://orcid.org/0000-0002-5782-0013
M. Lazar https://orcid.org/0000-0002-8508-5466
E. Boella https://orcid.org/0000-0003-1970-6794
G. Lapenta https://orcid.org/0000-0002-3123-4024

References

Agapitov, O. V., Wit, T. D. d., Mozer, F. S., et al. 2020, ApJL, 891, L20
Anderson, B. R., Skoug, R. M., Steinberg, J. T., & McComas, D. J. 2012, JGRA, 117, A04107
Bale, S. D., Badman, S. T., Bonnell, J. W., et al. 2019, Natur, 576, 237
Bale, S. D., Pulupa, M., Salem, C., Chen, C. H. K., & Quataert, E. 2013, ApJL, 769, L22
Berčič, L., Larson, D., Whittlesey, P., et al. 2020, ApJ, 892, 88
Berčič, L., Maksimović, M., Landi, S., & Matteini, L. 2019, MNRAS, 486, 3404
Boldyrev, S., & Horaites, K. 2019, MNRAS, 489, 3412
Cattell, C. A., Short, B., Breneman, A. W., & Grul, P. 2020, ApJ, 897, 126
Feldman, W. C., Asbridge, J. R., Bame, S. J., et al. 1976, JGR, 81, 5207
Feldman, W. C., Asbridge, J. R., Bame, S. J., Montgomery, M. D., & Gary, S. P. 1975, JGR, 80, 4181
Gary, S. P. 1978, PhPl, 20, 47
Gary, S. P., Feldman, W. C., Forslund, D. W., & Montgomery, M. D. 1975, JGR, 80, 4197
Gary, S. P., Scime, E. E., Phillips, J. L., & Feldman, W. C. 1994, JGR, 99, 23391
Gosling, J. T., Skoug, R. M., & Feldman, W. C. 2001, GeoRL, 28, 4155
Gurgiolo, C., Goldstein, M. L., Viñas, A. F., & Fazakerley, A. N. 2012, AnGeo, 30, 163
Halekas, J. S., Whittlesey, P., Larson, D. E., et al. 2020, ApJS, 246, 22
Hammond, C. M., Feldman, W. C., McComas, D. J., Phillips, J. L., & Forsyth, R. J. 1996, A&A, 316, 350
Horaites, K., Astfalk, P., Boldyrev, S., & Jenko, F. 2018, MNRAS, 480, 1499
Innocenti, M. E., Boella, E., Tenerani, A., & Velli, M. 2020, ApJL, 898, L41
Innocenti, M. E., Tenerani, A., Boella, E., & Velli, M. 2019a, ApJ, 883, 146
Innocenti, M. E., Tenerani, A., & Velli, M. 2019b, ApJ, 870, 66
Kasper, J. C., Bale, S. D., Belcher, J. W., et al. 2019, Natur, 576, 228
Kuzichev, I. V., Vasko, I. Y., Rualdo Soto-Chavez, A., et al. 2019, ApJ, 882, 81
Lacombe, C., Alexandrova, O., Matteini, L., et al. 2014, ApJ, 796, 5
Landi, S., & Pantellini, F. 2003, A&A, 400, 769
Lazar, M., Poedts, S., & Schlickeiser, R. 2011, MNRAS, 410, 663
López, R. A., Lazar, M., Shaaban, S. M., et al. 2019, ApJL, 873, L20
López, R. A., Lazar, M., Shaaban, S. M., Poedts, S., & Moya, P. S. 2020, ApJL, 900, L25
Maksimovic, M., Pierrard, V., & Lemaire, J. F. 1997, A&A, 324, 725
Maksimovic, M., Zouganelis, I., Chaufray, J. Y., et al. 2005, JGRA, 110, A09104
Malaspina, D. M., Halekas, J., Berčič, L., et al. 2020, ApJS, 246, 21
Markidis, S., Lapenta, G., & Rizwan-uddin 2010, Math. Comput. Simul., 80, 1509
Marsch, E. 2006, LRSP, 3, 1
Mozer, F. S., Agapitov, O. V., Bale, S. D., et al. 2020, ApJS, 246, 68
Ogilvie, K. W., & Scudder, J. D. 1978, JGR, 83, 3776
Pagel, C., Gary, S. P., de Koning, C. A., Skoug, R. M., & Steinberg, J. T. 2007, JGRA, 112, A04103
Phillips, J. L., & Gosling, J. T. 1990, JGR, 95, 4217
Pierrard, V., & Lemaire, J. 1996, JGR, 101, 7923
Pilipp, W. G., Miggenrieder, H., Montgomery, M. D., et al. 1987, JGR, 92, 1075
Roberg-Clark, G. T., Agapitov, O., Drake, J. F., & Swisdak, M. 2019, ApJ, 887, 190
Rosenbauer, H., Schwenn, R., Marsch, E., et al. 1977, JGZG, 42, 561
Salem, C., Hubert, D., Lacombe, C., et al. 2003, ApJ, 585, 1147
Scime, E. E., Bame, S. J., Feldman, W. C., et al. 1994, JGR, 99, 23401
Shaaban, S. M., Lazar, M., & Poedts, S. 2018, MNRAS, 480, 310
Spitzer, L., & Härm, R. 1953, PhRv, 89, 977
Stverák, v., Maksimovic, M., Trávníček, P. M., et al. 2009, JGRA, 114, A05104
Tang, B., Zank, G. P., & Kolobov, V. I. 2020, ApJ, 892, 95
Tong, Y., Vasko, I. Y., Pulupa, M., et al. 2019, ApJL, 870, L6
Vasko, I. Y., Krasnoselskikh, V., Tong, Y., et al. 2019, ApJL, 871, L29
Verscharen, D., Chandran, B. D. G., Jeong, S.-Y., et al. 2019, ApJ, 886, 136